Journal of Power Sources 641 (2025) 236839

Contents lists available at ScienceDirect

Journal of Power Sources

journal homepage: www.elsevier.com/locate/jpowsour

Chiral 2D flakes with single atoms inclusion for spin-controlled oxygen evolution

Denis Zabelin [a], Anastasiia Tulupova [a], Peter Švec [b], Alena Michalcova [c], Vasilii Burtsev [a], Marie Urbanova [d], Philipp Hönicke [e,f], Vladislav Buravets [a], Tomas Hrbek [g], Anastasiia Skvortsova [a], Anna Zabelina [a], Vaclav Svorcik [a], Stefan Michna [h], Jana Vejpravova [i], Oleksiy Lyutakov [a,*]

[a] Department of Solid State Engineering, University of Chemistry and Technology, 16628, Prague, Czech Republic
[b] Institute of Physics, Slovak Academy of Sciences, 845 11, Bratislava, Slovak Republic
[c] Department of Metals and Corrosion Engineering, University of Chemistry and Technology, 16628, Prague, Czech Republic
[d] Department of Physics and Measurements, University of Chemistry and Technology, 16628, Prague, Czech Republic
[e] Helmholtz-Zentrum Berlin (HZB), Hahn-Meitner Platz 1, 14109, Berlin, Germany
[f] Physikalisch-Technische Bundesanstalt (PTB), Abbestr. 2-12, 10587, Berlin, Germany
[g] Department of Surface and Plasma Science, Charles University, 180 00, Prague, Czech Republic
[h] Faculty of Mechanical Engineering, J. E. Purkyne University, 400 96, Usti nad Labem, Czech Republic
[i] Department of Condensed Matter Physics, Charles University, Prague 2, 12116, Czech Republic

HIGHLIGHTS

- Chiral 2D flakes (Ni:MoS_2) were prepared.
- The created material was used for spin-controlled electrochemistry.
- Created material allows reaching a good OER kinetic.
- The electron spin polarization ensures the suppression of hydrogen peroxide formation.
- Materials also shows excellent material stability.

ARTICLE INFO

Keywords:
MoS_2
Chiral 2D flakes
Single atom
Oxygen evolution
Spin-controlled chemistry

ABSTRACT

Spin control represents an interesting avenue in modern electrochemistry, with the ability to tune the state of reaction intermediates and the overall reaction selectivity and yield. One of the ways to achieve the reaction spin control is the preparation of specific electrodes through the utilization of the so-called chiral-induced spin selectivity phenomenon (CISS). This approach is based on the utilization of chiral coatings on the surface of redox-active materials, which allow one to align the spin of transited electrons, but limits the available current densities and electrode stability. In this work, the realization of the CISS phenomenon with the implementation of intrinsically chiral 2D flakes of MoS_2 doped with single Ni atoms is proposed for the first time. The created material was applied to an oxygen evolution reaction (OER) performed under alkaline conditions. The single-atom catalyst provides the material redox activity, while the flakes chirality ensures the alignment of the spins of transited electrons. We reached a significant enhancement of the OER kinetics and suppressed hydrogen peroxide formation. The utilization of the proposed chiral materials allows us to perform OER experiments at a relatively high current density and significantly improve the electrode stability.

* Corresponding author.
E-mail address: lyutakoo@vscht.cz (O. Lyutakov).

https://doi.org/10.1016/j.jpowsour.2025.236839
Received 9 December 2024; Received in revised form 25 February 2025; Accepted 18 March 2025
Available online 24 March 2025

1. Introduction

Spin control of electron transfer with the aim of tuning the reaction selectivity and yield is a hot topic in modern electrochemistry [1–5]. The use of spin-controlled electrochemistry allows tuning of the electrochemical reaction in the desired way, making it possible to realize enantioselective catalysis, adjust the reaction pathway, suppress the formation of undesired byproduct(s) and improve the reaction kinetics and yield [6–8]. Especially promising is the implementation of a spin-controlled chemistry in "challenging" reactions, based on multi-electron transitions [1,9]. In this sense, the use of spin-controlled electrochemistry in oxygen evolution, CO_2 or N_2 reduction can be mentioned as a few examples [1,10,11].

Among the above-mentioned reactions, the oxygen evolution reaction (OER) has been explored more widely and successfully. This is not surprising, since this half-reaction is an energy demanding process (due to a greater thermodynamic barrier compared to the other half reaction, e.g., hydrogen evolution), which represents a barrier for the broader deployment of water electrolysis [12–14]. In addition to the higher overpotential of OER and the high required pH values, the OER is also restricted by the undesired production of hydrogen peroxide [10,15,16]. This common by-product of the OER can lead to corrosion of electrolyser components [15,17]. The use of an electron current with "parallel" spins allows to align the spins of intermediate products (·OH radicals) and prohibits in this way their recombination in the form of hydrogen peroxide [3,18–20]. In particular, more energetically favourable and quantum allowable triplet oxygen is formed when electrons transit through the chiral electrode surface. This concept was recently demonstrated using a variety of materials, including various chiral coatings deposited on the electrode surface, or the utilization of intrinsically chiral redox-active nanomaterials or coatings [8,21–24].

The common design of the electrode with the ability of electron spin control includes the combination of high redox activity and externally or internally induced alignment of the transited electrons spins. This combination can be reached using an external magnetic field or redox-active ferromagnetic materials [10,25,26]. On the other hand, a spin alignment can be reached using chiral-induced spin selectivity (the so-called CISS phenomenon) [10,20,26–31]. In the CISS, the electron transition through the layer of chiral molecules results in the creation of a spin-polarized electric current [32–35]. CISS was efficiently employed in the OER, by coating of the electrode surface with various chiral organic molecules (cysteine, helicenes, etc.) [27,28,36]. Alternatively, the creation of "intrinsically chiral" electrodes, for example, using nanostructures self-assembling, was proposed for the same purposes [35,37–43]. As an example, the use of 2D chiral MoS_2 flakes (which serve simultaneously as a chiral spin valve and redox-active material) leads to an improvement in OER kinetics, decrease of the corresponding Tafel slope, and suppression of hydrogen peroxide production [39].

Apart from spin control, it should be noted that 2D materials could be considered as ideal candidates for immobilization of redox-active single atoms. In this case, the unusual environment of single atoms catalysts allows to increase their redox activity and simultaneously all single atoms are "in contact" with the surrounding electrolyte [44,45]. This approach was also recently combined with spin-controlled chemistry, using the creation of 2D ferromagnetic flakes (achiral Ni:MoS_2) and the additional utilization of an external magnetic field [26].

In this work, we propose the combination of the concept of a single-atom catalyst (embedded in 2D flakes) and chiral ensured spin selectivity for the increase of OER efficiency and the suppression of undesired hydrogen peroxide production. Both concepts have previously been reported separately but have not been combined up to now in the framework of single materials. In our assumption, the single-atom redox-active centers will ensure high catalytic activity, while the chiral structure of the surrounding 2D flakes will be responsible for the alignment of the spin of transferred electrons (including electrons transferred through redox-active centers), supporting the creation of triplet oxygen instead of undesired hydrogen peroxide. As a result of the proposed combination, an increase in material redox activity and stability was initially expected.

2. Experimental section

Detailed description of the materials used, samples preparation, and characterization is given in Supporting Information.

Preparation of chiral or nonchiral 1T-MoS_2 and Ni:1T-MoS_2 nanoflakes. Briefly, sodium molybdate dihydrate and 0.3 g of thioacetamide (CH_3CSNH_2) were dissolved in deionized water with or without the addition of nickel (II) nitrate hexahydrate and treated with ultrasonication for 30 min. Then L-ascorbic acid was added while stirring the solution and then nitrogen was flowed through the solution. The resulting solution was placed in a Teflon-lined stainless steel autoclave followed by heat treatment at 200 °C for 20 h. For the creation of nonchiral flakes, the obtained powder was immersed in NMP solution and then subjected to ultrasonic treatment for structure delamination. The chiral flakes were prepared by mixing Ni:1T-MoS_2 powder with cysteine solution in absolute ethanol and the suspension was subjected to ultrasonic treatment in an ice bath. The solid residue was collected by centrifugation and washed with absolute ethanol several times using repeated flakes centrifugation and re-dispersion.

3. Results and discussion

3.1. Main experimental concept

The schematic representation of the material preparation is presented in Fig. 1. First, the Ni:MoS_2 powder was synthesized using a hydrothermal approach. The amount of added Ni was optimized to reach its inclusion in the form of separated atoms. In the second step, the delamination of the created powder was performed with the use of ultrasonic treatment in the presence of chirality encoder – cysteine molecules. The delamination performed using the route previously reported by Gun'ko et al. [46] resulted in the creation of chiral 2D flakes with single-atom inclusions. For control experiments, the delamination of the flakes was performed without the addition of chirality encoders, and the flakes were used as prepared or after their post-preparative interaction with cysteine molecules. In all cases, flakes were deposited on the carbon electrode surface and used as OER catalysts under alkaline conditions. The main attention was focused on the OER efficiency as well as the suppression of undesired hydrogen peroxide production.

3.2. Characterization of chiral Ni:MoS_2 flakes

The characterization of the created structure is illustrated in Fig. 2. First, the measured UV–Vis spectra of Ni:MoS_2 flakes reveal the appearance of a strong absorption band with a similar spectral position for all flakes independently of their expected chirality or its absence.

CD measurements indicate the appearance of two distinct peaks, located at 270 and 320 nm. These peaks are symmetric with respect to the wavelength axis and their appearance and sign are determined by the used enantiomer chirality (L- or D-cysteine molecules). We did not observe the CD signal (nonzero) at wavelengths above 400 nm (unlike [46]). However, the Cotton effect was observed at shorter wavelengths, where both chiral and nonchiral flakes (prepared without cysteine addition) exhibit the intrinsic absorption band. The observed CD signal cannot be attributed to cysteine, since cysteine absorbs at shorter wavelengths. The formation of Mo complexes with cysteine is also less probable, as it should have led to surface passivation and a decrease in catalytic activity (which contradicts the results of electrochemistry discussed below). On the other hand, after the flakes washing, we did not observe Raman peaks of cysteine (although XPS showed some signal from the S-R bond, Figs. S1 and S2). The preparation of flakes without cysteine addition results in a closed-to-zero CD signal. The calculated

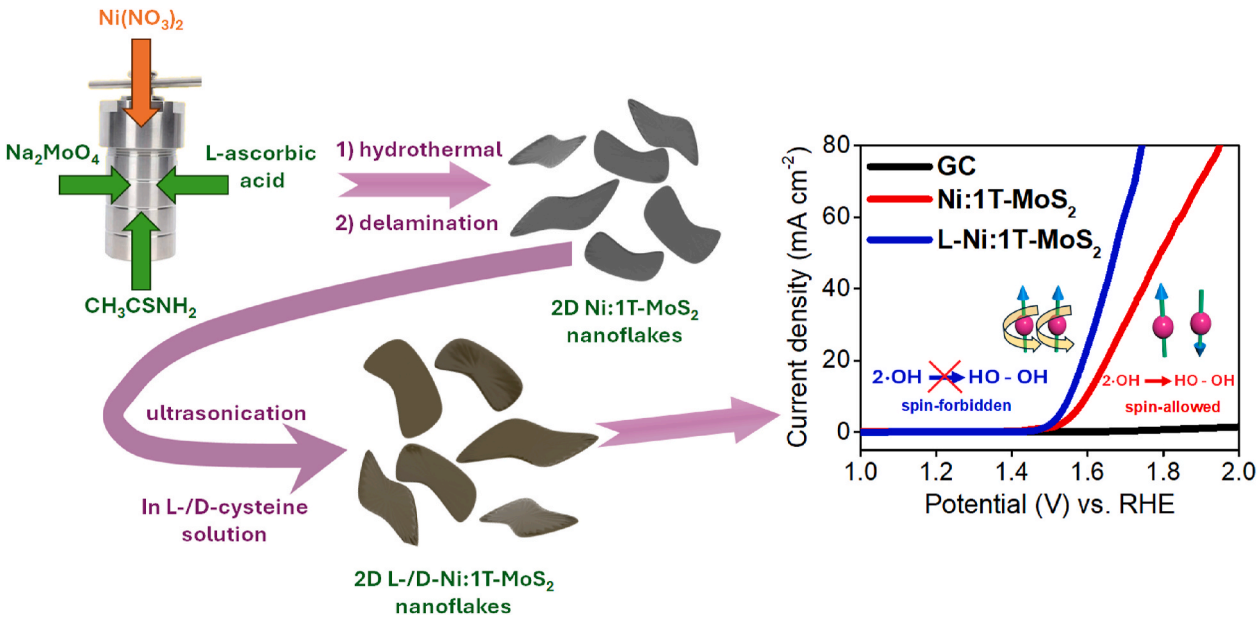

Fig. 1. Schematic representation of the preparation of chiral flakes: solvothermal synthesis with the inclusion of single-atom redox-active centers, flakes delamination in the presence of the chirality encoder and creation of chiral 2D flakes with single atom inclusion, flakes participation in OER with enhanced triplet oxygen production and suppression of hydrogen peroxide production.

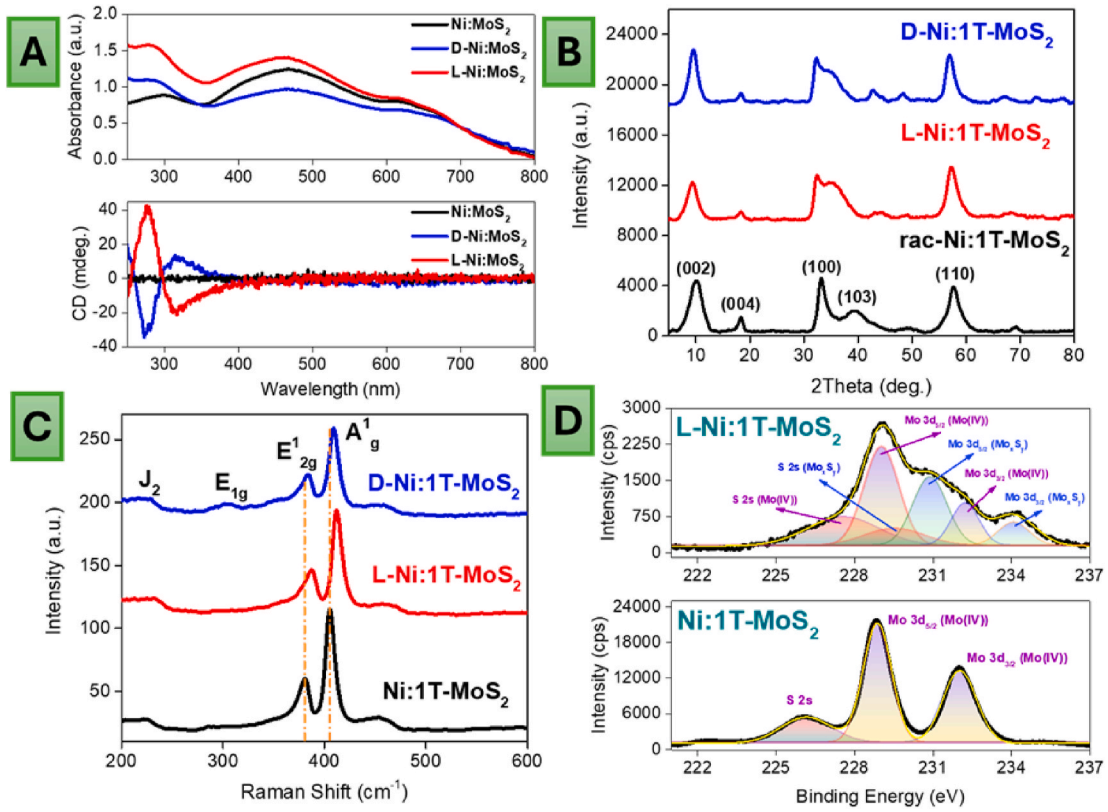

Fig. 2. (A) – UV–Vis and CD spectra of chiral and nonchiral flakes; (B), (C) – XRD patterns and Raman spectra of Ni:MoS_2, L-Ni:MoS_2, and D-Ni:MoS_2 flakes; (D) – deconvolution of the Mo-related region of the XPS spectrum (chiral L-Ni:MoS_2 vs nonchiral Ni:MoS_2 flakes).

values of the g-factor for both L-Ni:MoS_2 and D-Ni:MoS_2 were $0.78{\cdot}10^{-3}$ and $0.88{\cdot}10^{-3}$ at 275 nm and $0.45{\cdot}10^{-3}$ and $0.4{\cdot}10^{-3}$ at 315 nm. Importantly, the observed CD response cannot arise from cysteine molecules (the apparent CD signal of cysteine was observed at 220 nm – Fig. S3) and should be attributed to the intrinsic chirality of the flakes (Fig. 2A vs. Fig. S3). It should also be noted that our results correlate with those of several previous works, where the same route of chiral 2D transition metals chalcogenides creation was proposed [46,47].

In the next step, the crystalline structure of the created flakes was analysed by X-ray diffraction (XRD). XRD patterns clearly indicate that Ni atoms are embedded in the metallic 1T phase of MoS_2 (see Fig. S4, JCPDS No.75-1539, the diffraction peak (002) is shifted due to the larger

interlayer distance). Such a phase can ensure excellent charge mobility between the charge source and the redox-active Ni atoms (the experimental route was optimized to obtain even this phase, taking into account its "metal-like" behaviour). Furthermore, the 1T structure of the created flakes is conserved even during delamination in the presence of chirality encoders (Fig. 2B). Furthermore, HAADF-STEM measurements also confirm the creation of the 1T structure of the created 2D flakes (Fig. S5). In the XRD patterns, no cysteine reflexes are observed (on the washed flakes, some peaks of cysteine can be detected on "unwashed flakes" - Fig. S6). The Raman spectrum of exfoliated Ni:MoS_2 flakes shows two main Raman-active modes, E^1_{2g} and A_{1g} located at 370 and 405 cm^{-1} corresponding to in-plane and out-of-plane lattice vibrations, respectively [48–50] (Fig. 2C). The blue shift of the E^1_{2g} mode observed for chiral flakes indicates a lattice compression [48], probably introduced by grafted or intercalated cysteine molecules and related flakes distortion. The simultaneous blue shift of the A^1_g mode indicates an increased contribution from vdW forces, appearing in the case of a stronger stacking of chiral flakes.

The survey XPS spectra indicate the apparent changes in the surface composition of flakes prepared with or without chirality encoder addition (Fig. S7). An apparent increase in carbon concentration and the screening of Mo and Ni signals were observed for chiral flakes, indicating that cysteine molecules are attached to the flakes even after careful flakes watching (this result was also confirmed by high-resolution XPS of the characteristic sulfur signal – Fig. S1). In addition, detailed XPS scans of Mo (Fig. 2D) reveal changes in its chemical state (evident from a slight shift of characteristic peaks toward higher energies), indicating some appearance of Mo (VI) [51]) and the formation of nonstoichiometric material after flakes delamination in the presence of cysteine. In particular, the appearance of a characteristic peak of Mo_xS_y is observed, indicating the partial removal of Mo (or sulfur) atoms during the preparation of the chiral flakes. The creation of a nonstoichiometric composition (i.e., vacancies on the 2D flakes surface) and changes in the Mo oxidation state accompanied by lattice distortion can be considered as a source of chirality (in the case of flakes delamination in the presence of cysteine molecules).

The distribution of Ni, Mo, and S atoms was measured using the HAADF-HRTEM technique. The results obtained show the homogeneous distribution of Ni atoms in the structure of flakes delaminated either in a classical (ultrasound-assisted) way or in the presence of the chirality encoder (Fig. 3A and B). The spatial arrangement of Ni atoms corresponds well with those of Mo and S, while a formation of Ni clusters is not observed, suggesting that Ni was indeed introduced in the form of single atoms. The redox state of Ni was analysed using X-ray absorption fine structure spectroscopy (XAFS - Fig. 3C). Comparison of the results obtained with L-Ni:MoS_2 flakes and reference data [52] from Ni foil measurements leads to the conclusion that Ni atoms are mainly bound in a mixed $3^+/2^+$ oxidation state, which can ensure the good catalytic activity of single Ni atoms through the electron reception/donation during the transition between oxidation states. The 2D nature of the flakes was confirmed by SEM (Fig. S8) and AFM techniques (Fig. 3D and E). The SEM revealed apparent changes between the Ni:MoS_2 shapes before and after delamination (Fig. S8 vs. S9); however, no apparent differences were indicated between the delaminated chiral and nonchiral materials. More detailed AFM measurements reveal a higher thickness of chiral flakes compared to nonchiral flakes (5 against 6 nm). This difference can be attributed to the presence of intercalated cysteine molecules. In addition, the surface geometry of nonchiral flakes was

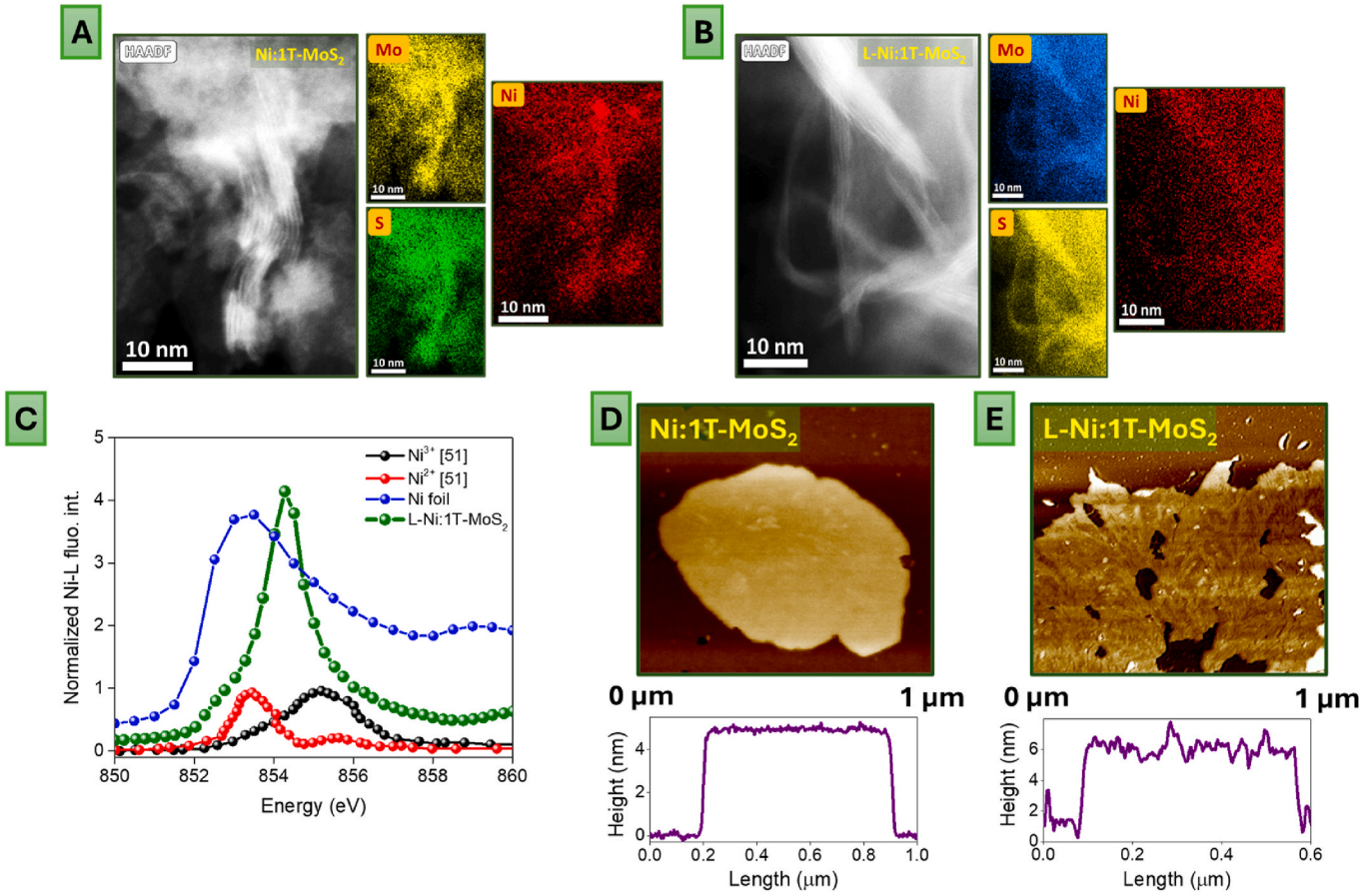

Fig. 3. (A), (B) – HAADF/HRTEM images of chiral and nonchiral Ni:MoS_2 flakes and the corresponding spatial distribution of particular elements; (C) – XAFS measurement results (including control and reference data), revealing the state of embedded single Ni atoms; (D), (E) – AFM images and profiles of nonchiral and chiral L-Ni:1T-MoS_2 flakes.

found to be atomically flat, whereas apparent morphological features were observed for chiral flakes. This surface morphology deviation was the same for L- and D-chiral flakes (Fig. S10) and was found to be statistically relevant (Fig. S11). Such deviation of flakes morphology correlates well with changes in surface chemistry and increased in-plane stress (evident from XPS and Raman measurements) and can be attributed to the distortion of surface atoms (potentially related to the appearance of chirality). Therefore, the results of material(s) characterization confirm the creation of chiral 2D materials with a homogeneous distribution of single Ni atom inclusions.

Finally, we also performed magnetic measurements of the prepared flakes (Figs. S12 and S13). However, ferromagnetic behaviour was not observed, which is expected otherwise, since spin orientation occurs in the case of an electric current flowing through the material and not in the case of the material itself (i.e., spins of transited electrons can be aligned, not the spins of 'intrinsic' material electrons) [53].

3.3. OER under alkaline conditions

In the next step, we proceed to the utilization of this material for OER, performed under alkaline conditions. First, the kinetics of the OER was measured using the linear sweep voltammetry (LSV) approach as a function of the chirality of the materials (Fig. 4A). The on-set potential for the OER was found to be near 1.48 V vs. RHE for Ni:MoS_2 and independent of the chirality of the flakes. Significantly worse catalytic activity was observed for MoS_2 flakes without the incorporation of redox-active single atoms (Fig. 4A). The apparent impact of flake chirality on the material redox activity is evident from the shape of the LSV curve. In the case of chiral flakes, a sharper increase in current density with an applied potential is visible. The shape of L- or D-chiral flakes was the same, so the observed phenomenon is typical for a chiral material and independent of its left- or right-handling nature. In particular, the overpotential required for the 50 mA·cm^{-2} current density was 1.79 V (vs. RHE) for nonchiral flakes and decreased to 1.66 and 1.67 V for L- or D-chiral flakes respectively. It should be also noted that in LSV curves we achieved a current density close to 100 mV·cm^{-2}. With the use of chiral flakes, higher current density values of up to 350 mA·cm^{-2} can be achieved (Fig. S14). However, in this case, the LSV measurements were complicated by the formation and detachment of oxygen bubbles, which led to fluctuations in the LSV curve.

The shape of the LSV curves also reflects itself in the values of the Tafel slope (Fig. 4B). In particular, we observed 279 mV/dec for MoS_2

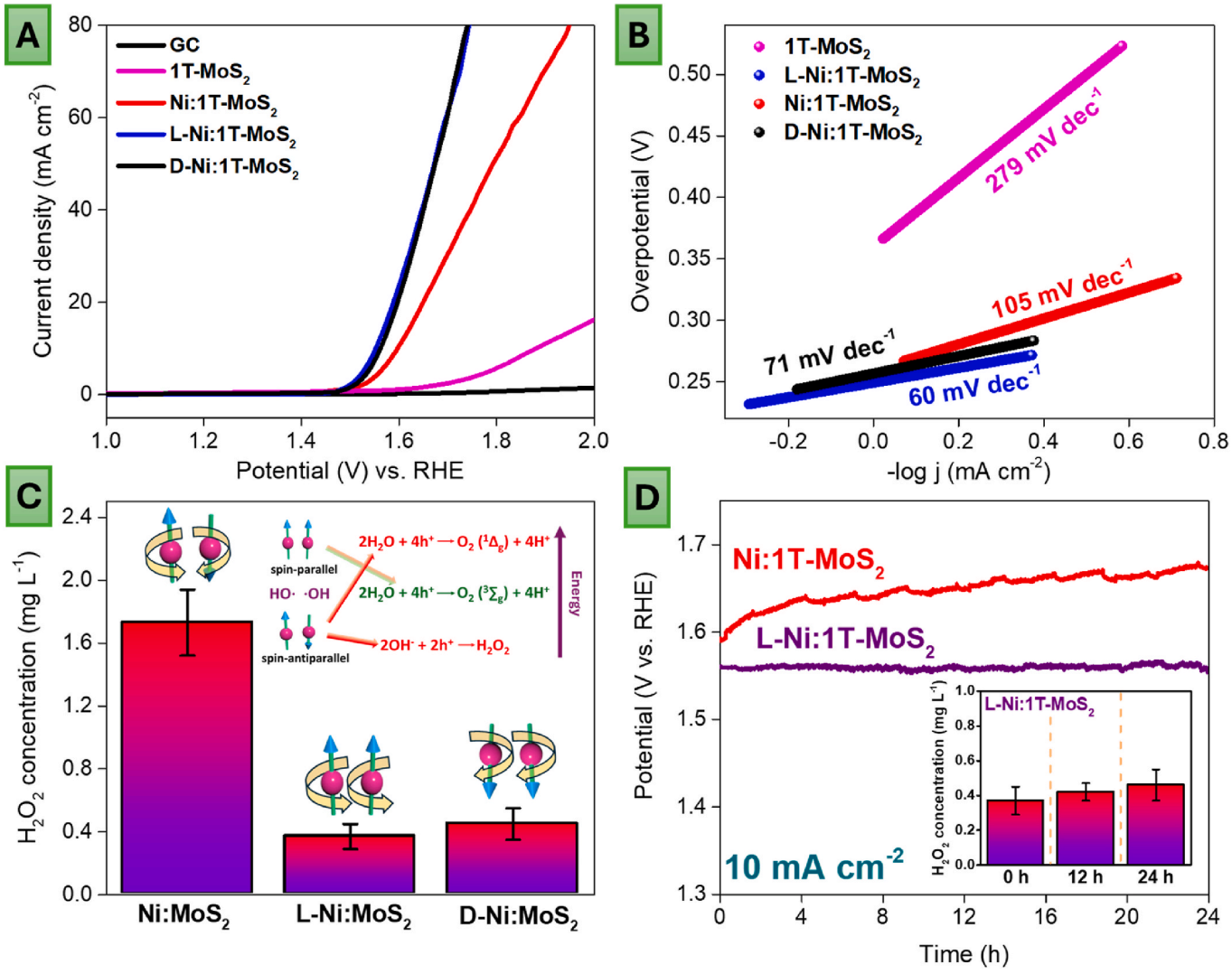

Fig. 4. (A) – LSV curves measured in OER potentials with the use of chiral and nonchiral flakes (carbon electrode and delaminated MoS_2 flakes are added as controls); (B) – calculated from LSV values of Tafel slopes for particular materials; (C) – amounts of hydrogen peroxide produced during OER with the use of nonchiral and chiral Ni:MoS_2 flakes (insert shows the impact or spin polarization on OER reaction); (D) – stability tests performed in constant current density regime and amounts of "undesired" hydrogen peroxide produced (measured after electrolyte exchange using 25 mA/cm^2 current density) during stability test.

fakes without single Ni atoms. This value decreased to 105 mV.dec^{-1} after the introduction of single-atom redox-active centers and further decreased after the creation of chiral flakes to 60–70 mV.dec^{-1}. An additional control experiment is also presented in Fig. S15. In this case, we used the simple coating of intrinsically nonchiral Ni:MoS_2 flakes with chiral cysteine molecules. Measured LSV curves indicate the lower catalytic activity of the materials compared to that of intrinsically chiral flakes prepared by using the chirality encoding at the stage of flakes delamination. Similar results were obtained with the use of Ni:1T-MoS_2 flakes delaminated in cysteine racemate. In this case, lower redox activity (Fig. S16) and relatively high peroxide production (Fig. S17) were observed and can be attributed to the absence of flakes chirality (Fig. S18). Thus, the CISS effect observed in the main experiments should be attributed rather to intrinsic flakes chirality than to organic enantiomers coatings.

To further compare the redox properties of the chiral (L-Ni:1T-MoS_2) and nonchiral (Ni:1T-MoS_2) flakes, we calculated the mass activity and the specific surface activity (Table S1). In the case of mass activity, we observed the significant difference: 65.1 A·g^{-1} and 240.3 A·g^{-1} for nonchiral and chiral flakes, which revealed a nearly three-fold increase in the flakes activity when chirality is introduced. However, such a difference can also be attributed to a greater material-electrolyte contact area due to the deviation of the chiral flakes' morphology from the flat one (evident from AFM images, Fig. 3D and E). Therefore, in the next step, the electrochemically active surface areas (ECSA) of the chiral and nonchiral flakes were calculated (Fig. S19) and found to be 0.53 cm^{-2} (Ni:1T-MoS_2) and 0.83 cm^{-2} (L-Ni:1T-MoS_2). Subsequently, the determined values of the specific surface activity were found to be 0.52 mA·cm^{-2} and 0.82 mA·cm^{-2} accordingly. Therefore, even in this case, the increase in chiral material redox activity is evident, but not as pronounced as in the case of mass activity calculation (the differences observed in the previous case of mass activity should be partially attributed to the increased surface area of chiral flakes).

Subsequently, we performed a range of hydrogen peroxide tests with the use of chiral and nonchiral flakes. In this case, the samples were used for water splitting (OER was carried out on the electrode coated with chiral or nonchiral flakes in the chronopotentiometry regime (with a constant current density of 25 m·Acm^{-2}) for 30 min. After the experiment, part of the electrolyte solution was taken away and the amounts of hydrogen peroxide produced were analysed using the calibration curves (Fig. S20). The results obtained are presented in Fig. 4C as a concentration of detected peroxide. One can see that the use of chiral flakes approximately suppresses the production of undesired hydrogen peroxide 3.3 times, as was originally expected. In a common case, the reaction of the hydroxyl anion on the surface of the electrode can result in the formation of ·OH radicals or the production of oxygen. In turn, the ·OH radicals (with randomly oriented spins) can combine with the creation of hydrogen peroxide, as shown in Fig. 4C (insert). In our case, suppression of hydrogen peroxide production was observed, which should be attributed to the CISS effect. In particular, the involvement of electrons with parallel spins results in the alignment of ·OH radicals spins. Radicals with alignment spin cannot recombine with the formation of hydrogen peroxide (since hydrogen peroxide is a diamagnetic molecule). Therefore, the only reaction pathway for short-lived ·OH radicals is the formation of paramagnetic oxygen (Fig. 4C, insert), which is the mechanism that suppresses the accumulation of peroxide in the reaction mixture [3,8,20,27,28,32,39,41,54–64].

We also performed a range of stability tests under the constant current density regime (10 10 mA·cm^{-2}). In the case of nonchiral flakes, the apparent increase of the potential required to keep the current density at the desired level was observed (Fig. 4D). This fact reveals a clear decrease in the catalytic activity of nonchiral Ni:1T-MoS_2 flakes, which may be associated with the negative influence of the peroxide produced, which can damage the redox-active material (Fig. S21). However, in the case of chiral L-Ni:1T-MoS_2 flakes (Fig. 4D), as well as in the case of D-Ni:1T-MoS_2 flakes (Fig. S22), we need not increase the potential required to keep the current density at a constant level during 24 h of operation. Furthermore, the measured amount of hydrogen peroxide produced at the beginning of chiral samples stability tests and after 12 or 24 h of their utilization also remains at the same low level, indicating that the CISS effect and the related suppression of hydrogen peroxide formation are stable during the long-term utilization of the created material. This fact should be attributed to the conservation of the CISS effect and should confirm the survival of flakes chirality. Additional measurements of the morphology, composition, and crystallinity of the chiral flakes after stability tests indicate slight changes in both parameters (Figs. S23 and S24). A similar situation was also observed in the case of nonchiral flakes (Figs. S25 and S26). Similar results were obtained with the use of XPS measurements, which indicate the absence of apparent changes in the chemical states of the Mo, S, and Ni atoms (Fig. S27 vs Fig. 2 and Fig. S1).

In the next step, we compare our results with previously published, and the results are summarized in Table 1 [3,8,20,27,28,32,39,41,54–64]. In this regard, it should be noted that part of the OER reactions with the utilization of the CISS phenomenon are performed using chiral coatings deposited on the surface of redox-active materials. This approach gives a good result in the case of OER but clearly is significantly limited by the maximal reported values of the current density. This is not surprising, since the use of a high current density or long-term electrode utilization can lead to the destruction of the chiral coating, thereby neutralizing the CISS effect. These disadvantages were overcome by the utilization of intrinsically chiral materials, where significantly higher current densities were sometimes reported, including our work. We assume that the introduction of chirality through the intrinsic chirality of 2D structures makes it possible to achieve higher current densities, as well as good stability of the material and a lasting CISS effect. Furthermore, the introduction of single atoms leads to a significant decrease in the value of the Tafel slope, compared to most of previously published works (Table 1). Finally, it should be noted that our

Table 1
Comparison of our results reached with CISS utilization with previously published ones (utilization of chiral coatings and intrinsically chiral materials).

Material	Maximum Current Density, mA cm^{-2}	Tafel slope, mV dec^{-1}	Time of stability	Ref.
Chiral-coated materials				
Ni/Al/D-Phe	≈39	129	2000 s	[52]
Au-Ni bilayer/L-cysteine	≈20	114	4500 s	[55]
NiO_x/Au/thiadiazole-[7]helicene	≈18	–	1800 s	[27]
Fe_3O_4@L-tryptophan	≈20	–	6000 s	[20]
TiO_2@chiral DNA	≈0.3	–	–	[3]
Chiral Zn porphyrins	≈6·10^{-3}	–	2400 s	[28]
Intrinsically Chiral Materials				
$NiFeO_x$ catalyst/TiO_2/PTAA/chiral 2D OIHPs/Mo:$BiVO_4$/SnO_2/ITO	≈2.84 (photocurrent)	–	–	[56]
TiS_2@DTA	≈5.8	–	–	[57]
S-MBA_MoS_2	≈7.5	395	2500 s	[39]
23 % Fe-doped L-Co_3O_4	≈67	34	–	[32]
Chiral Fe_3O_4 (L-tartaric acid)	≈38	120	10000 s	[58]
L-CoO_x	≈60	–	250 s	[60]
L-CuO	≈13	117	–	[8]
s-Fe_3O_4/chiral + H_{ext} ON	≈1.7	–	24 h	[61]
L-ZnO	≈0.45	–	–	[62]
CdSe@CP	≈10.5·10^{-3}	–	3600 s	[63]
L-TA-FeNi CP	≈400	45.4	100 h	[41]
Co@CoO-L	≈120	84.2	20 h	[64]
TiS_2_R-PEA_PEG	≈115	306	–	[54]
L-Ni:1T-MoS_2	80	60	10 h	This work

work demonstrates that, by generating spin-polarized electrons, it is possible to increase the efficiency of the electrochemical reaction (OER in our case) and extend the lifetime of redox-active material(s). Indeed, a similar approach can be further used in the case of alternative 2D materials or nanomaterials with single-atom inclusion or with other redox-active sites.

4. Conclusion

Chiral 2D flakes (MoS_2) with inclusion of single Ni atoms were prepared by solvothermal synthesis and subsequent material delamination in the presence of chirality encoder (cysteine enantiomers). The proposed approach allows us to create chiral 2D materials with a single atom inclusion, combining in this way the redox activity (ensured by single atoms) and spin polarization of transited electrons. After the structure and chirality conformation, the created material was used for spin-controlled electrochemistry. The presence of a single-atom catalyst allows reaching a good OER kinetic, while the electron spin polarization induced by CISS ensures the suppression of hydrogen peroxide formation (due to the spin alignment of intermediate OH^- radicals). Furthermore, the Tafel slope values decreased from 105 to 60 mV dec^{-1} (L-Ni:1T-MoS_2) after the introduction of chirality. The amount of undesired peroxide production also decreased by a factor of about 3.3, compared to the nonchiral Ni:MoS_2. Control experiments with a "simple" cysteine coating indicate that the enhancement of the kinetics of OER should be attributed rather to "intrinsic" flakes chirality. The proposed concept (CISS, achieved with the utilization of intrinsically chiral 2D material and single catalyst inclusion) allows us to reach higher (compared to previously reported cases) current densities and excellent material stability in terms of both redox activity and long-term suppression of hydrogen peroxide formation.

CRediT authorship contribution statement

Denis Zabelin: Writing – review & editing, Methodology, Investigation, Data curation, Conceptualization. **Anastasiia Tulupova:** Validation, Methodology, Investigation. **Peter Švec:** Investigation. **Alena Michalcova:** Investigation. **Vasilii Burtsev:** Investigation. **Marie Urbanova:** Investigation, Data curation. **Philipp Hönicke:** Investigation, Data curation. **Vladislav Buravets:** Investigation. **Tomas Hrbek:** Investigation. **Anastasiia Skvortsova:** Investigation. **Anna Zabelina:** Investigation. **Vaclav Svorcik:** Writing – review & editing, Funding acquisition, Formal analysis, Data curation. **Stefan Michna:** Investigation. **Jana Vejpravova:** Data curation, Investigation. **Oleksiy Lyutakov:** Writing – review & editing, Supervision, Data curation, Conceptualization.

Declaration of competing interest

The authors declare that they have no known competing financial interests or personal relationships that could have appeared to influence the work reported in this paper.

Acknowledgement

This work was supported by the GACR under project 23-051197S, by the Project OP JAK_Amulet, No CZ.02.01.01/00/22_008/0004558, of the Ministry of Education, Youth and Sports, which is co-funded by the European Union. The authors acknowledge CERIC-ERIC Consortium for access to experimental facilities at LRI SPL-HTC in Prague (Proposal number: 20237251). Work realization received support of Slovak Research and Development Agency for Science, project APVV-19-0369 and Scientific Grant Agency of the Ministry of Education, Science, Research and Sport of the Slovak Republic and Slovak Academy of Sciences, project VEGA 2/0144/21. The work was partially supported by the OP VVV Project NANOTECH ITI II. No. CZ.02.1.01/0.0/0.0/18_069/0010045 (S.M.). We acknowledge MGML (mgml.eu), supported within the program of Czech Research Infrastructures (project no. LM2023065), for providing access to the low-temperature facilities to carry out magnetic experiments (J.V.). We also acknowledge MGML (mgml.eu), supported within the program of Czech Research Infrastructures (project no. LM2023065), for providing access to the low-temperature facilities to carry out magnetic experiments.

Appendix A. Supplementary data

Supplementary data to this article can be found online at https://doi.org/10.1016/j.jpowsour.2025.236839.

Data availability

The data that support the findings of this study are openly available in Zenodo at https://doi.org/10.5281/zenodo.13221852.

References

[1] Y. Sang, F. Tassinari, K. Santra, W. Zhang, C. Fontanesi, B.P. Bloom, D.H. Waldeck, J. Fransson, R. Naaman, Chirality enhances oxygen reduction, Proc. Natl. Acad. Sci. 119 (2022) e2202650119, https://doi.org/10.1073/pnas.2202650119.
[2] Y. Liang, M. Lihter, M. Lingenfelder, Spin-control in electrocatalysis for clean energy, Isr. J. Chem. 62 (2022) e202200052, https://doi.org/10.1002/ijch.202200052.
[3] W. Mtangi, V. Kiran, C. Fontanesi, R. Naaman, Role of the electron spin polarization in water splitting, J. Phys. Chem. Lett. 6 (2015) 4916–4922, https://doi.org/10.1021/acs.jpclett.5b02419.
[4] B.P. Bloom, Y. Lu, T. Metzger, S. Yochelis, Y. Paltiel, C. Fontanesi, S. Mishra, F. Tassinari, R. Naaman, D.H. Waldeck, Asymmetric reactions induced by electron spin polarization, Phys. Chem. Chem. Phys. 22 (2020) 21570–21582, https://doi.org/10.1039/D0CP03129A.
[5] P. Bainova, J.-P. Joly, M. Urbanova, D. Votkina, M. Erzina, B. Vokata, A. Trelin, P. Fitl, G. Audran, N. Vanthuyne, J. Vinklarek, V. Svorcik, P. Postnikov, S.R. A. Marque, O. Lyutakov, Plasmon-assisted chemistry using chiral gold helicoids: toward asymmetric organic catalysis, ACS Catal. 13 (2023) 12859–12867, https://doi.org/10.1021/acscatal.3c02958.
[6] L. Pan, M. Ai, C. Huang, L. Yin, X. Liu, R. Zhang, S. Wang, Z. Jiang, X. Zhang, J.-J. Zou, W. Mi, Manipulating spin polarization of titanium dioxide for efficient photocatalysis, Nat. Commun. 11 (2020) 418, https://doi.org/10.1038/s41467-020-14333-w.
[7] T.S. Metzger, S. Mishra, B.P. Bloom, N. Goren, A. Neubauer, G. Shmul, J. Wei, S. Yochelis, F. Tassinari, C. Fontanesi, D.H. Waldeck, Y. Paltiel, R. Naaman, The electron spin as a chiral reagent, Angew. Chem. 132 (2020) 1670–1675, https://doi.org/10.1002/ange.201911400.
[8] Y. Jin, W. Fu, Z. Wen, L. Tan, Z. Chen, H. Wu, P. Wang, Chirality engineering of colloidal copper oxide nanostructures for tailored spin-polarized catalysis, J. Am. Chem. Soc. 146 (2024) 2798–2804, https://doi.org/10.1021/jacs.3c12965.
[9] A. Zabelina, E. Miliutina, J. Dedek, A. Trelin, D. Zabelin, R. Valiev, R. Ramazanov, V. Burtsev, D. Popelkova, M. Stastny, V. Svorcik, O. Lyutakov, Nitrogen photoelectrochemical reduction on TiB_2 surface plasmon coupling allows us to reach enhanced efficiency of ammonia production, ACS Catal. 13 (2023) 10916–10926, https://doi.org/10.1021/acscatal.3c03210.
[10] R. Naaman, Y. Paltiel, D.H. Waldeck, Chiral induced spin selectivity gives a new twist on spin-control in chemistry, Acc. Chem. Res. 53 (2020) 2659–2667, https://doi.org/10.1021/acs.accounts.0c00485.
[11] Y. Jiang, K. Yang, M. Li, D. Xu, Z. Ma, Engineering the spin configuration of electrocatalysts for electrochemical renewable conversions, Mater. Chem. Front. 8 (2024) 528–552, https://doi.org/10.1039/D3QM00841J.
[12] M. Grätzel, Photoelectrochemical cells, Nature 414 (2001) 338–344, https://doi.org/10.1038/35104607.
[13] M. El ouardi, A. El Idrissi, M. Arab, M. Zbair, H. Haspel, M. Saadi, H. Ait Ahsaine, Review of photoelectrochemical water splitting: from quantitative approaches to effect of sacrificial agents, oxygen vacancies, thermal and magnetic field on (photo)electrolysis, Int. J. Hydrogen Energy 51 (2024) 1044–1067, https://doi.org/10.1016/j.ijhydene.2023.09.111.
[14] D. Zabelin, A. Zabelina, E. Miliutina, A. Trelin, R. Elashnikov, D. Nazarov, M. Maximov, Y. Kalachyova, P. Sajdl, J. Lancok, M. Vondracek, V. Svorcik, O. Lyutakov, Design of hybrid Au grating/TiO_2 structure for NIR enhanced photoelectrochemical water splitting, Chem. Eng. J. 443 (2022) 136440, https://doi.org/10.1016/j.cej.2022.136440.
[15] J. Liu, Y. Liu, N. Liu, Y. Han, X. Zhang, H. Huang, Y. Lifshitz, S.-T. Lee, J. Zhong, Z. Kang, Metal-free efficient photocatalyst for stable visible water splitting via a two-electron pathway, Science 347 (2015) 970–974, https://doi.org/10.1126/science.aaa3145.
[16] D. Zabelin, K. Severa, J. Kuliček, B. Rezek, A. Tulupova, R. Elashnikov, A. Zabelina, V. Burtsev, P. Sajdl, E. Miliutina, V. Svorcik, O. Lyutakov, Creation and plasmon-assisted photosensitization of annealed Z-schemes for sunlight-only water splitting,

ACS Appl. Mater. Interfaces 15 (2023) 29072–29083, https://doi.org/10.1021/acsami.3c02884.
[17] J.A. Seabold, K.-S. Choi, Effect of a cobalt-based oxygen evolution catalyst on the stability and the selectivity of photo-oxidation reactions of a WO_3 photoanode, Chem. Mater. 23 (2011) 1105–1112, https://doi.org/10.1021/cm1019469.
[18] P.C. Mondal, W. Mtangi, C. Fontanesi, Chiro-spintronics: spin-dependent electrochemistry and water splitting using chiral molecular films, Small Methods 2 (2018) 1700313, https://doi.org/10.1002/smtd.201700313.
[19] H. Gajapathy, S. Bandaranayake, E. Hruska, A. Vadakkayil, B.P. Bloom, S. Londo, J. McClellan, J. Guo, D. Russell, F.M.F. de Groot, F. Yang, D.H. Waldeck, M. Schultze, L. Robert Baker, Spin polarized electron dynamics enhance water splitting efficiency by yttrium iron garnet photoanodes: a new platform for spin selective photocatalysis, Chem. Sci. 15 (2024) 3300–3310, https://doi.org/10.1039/D3SC03016D.
[20] W. Zhang, K. Banerjee-Ghosh, F. Tassinari, R. Naaman, Enhanced electrochemical water splitting with chiral molecule-coated Fe_3O_4 nanoparticles, ACS Energy Lett. 3 (2018) 2308–2313, https://doi.org/10.1021/acsenergylett.8b01454.
[21] Z. Xue, B. Wu, Z. Zhang, C. Lin, X. Li, Q. Zhang, K. Tao, Spin selectivity induced by the interface effect for boosted water oxidation, ACS Catal. 14 (2024) 5685–5695, https://doi.org/10.1021/acscatal.4c00142.
[22] F.A. Garcés-Pineda, M. Blasco-Ahicart, D. Nieto-Castro, N. López, J.R. Galán-Mascarós, Direct magnetic enhancement of electrocatalytic water oxidation in alkaline media, Nat. Energy 4 (2019) 519–525, https://doi.org/10.1038/s41560-019-0404-4.
[23] F. Davodi, E. Mühlhausen, M. Tavakkoli, J. Sainio, H. Jiang, B. Gökce, G. Marzun, T. Kallio, Catalyst support effect on the activity and durability of magnetic nanoparticles: toward design of advanced electrocatalyst for full water splitting, ACS Appl. Mater. Interfaces 10 (2018) 31300–31311, https://doi.org/10.1021/acsami.8b08830.
[24] Q. Huang, H. Sheng, Magnetic-field-induced spin regulation in electrocatalytic reactions, Chem. Eur J. 30 (2024) e202400352, https://doi.org/10.1002/chem.202400352.
[25] Q. Huang, S. Xie, J. Hao, Z. Ding, C. Zhang, H. Sheng, J. Zhao, Spin-enhanced O−H cleavage in electrochemical water oxidation, Angew. Chem. Int. Ed. 62 (2023) e202300469, https://doi.org/10.1002/anie.202300469.
[26] T. Sun, Z. Tang, W. Zang, Z. Li, J. Li, Z. Li, L. Cao, J.S. Dominic Rodriguez, C.O. M. Mariano, H. Xu, P. Lyu, X. Hai, H. Lin, X. Sheng, J. Shi, Y. Zheng, Y.-R. Lu, Q. He, J. Chen, K.S. Novoselov, C.-H. Chuang, S. Xi, X. Luo, J. Lu, Ferromagnetic single-atom spin catalyst for boosting water splitting, Nat. Nanotechnol. 18 (2023) 763–771, https://doi.org/10.1038/s41565-023-01407-1.
[27] Y. Liang, K. Banjac, K. Martin, N. Zigon, S. Lee, N. Vanthuyne, F.A. Garcés-Pineda, J.R. Galán-Mascarós, X. Hu, N. Avarvari, M. Lingenfelder, Enhancement of electrocatalytic oxygen evolution by chiral molecular functionalization of hybrid 2D electrodes, Nat. Commun. 13 (2022) 3356, https://doi.org/10.1038/s41467-022-31096-8.
[28] W. Mtangi, F. Tassinari, K. Vankayala, A. Vargas Jentzsch, B. Adelizzi, A.R. A. Palmans, C. Fontanesi, E.W. Meijer, R. Naaman, Control of electrons' spin eliminates hydrogen peroxide formation during water splitting, J. Am. Chem. Soc. 139 (2017) 2794–2798, https://doi.org/10.1021/jacs.6b12971.
[29] R. Naaman, D.H. Waldeck, Chiral-induced spin selectivity effect, J. Phys. Chem. Lett. 3 (2012) 2178–2187, https://doi.org/10.1021/jz300793y.
[30] R. Naaman, D.H. Waldeck, Spintronics and chirality: spin selectivity in electron transport through chiral molecules, Annu. Rev. Phys. Chem. 66 (2015) 263–281, https://doi.org/10.1146/annurev-physchem-040214-121554.
[31] B.P. Bloom, Y. Paltiel, R. Naaman, D.H. Waldeck, Chiral induced spin selectivity, Chem. Rev. 124 (2024) 1950–1991, https://doi.org/10.1021/acs.chemrev.3c00661.
[32] A. Vadakkayil, C. Clever, K.N. Kunzler, S. Tan, B.P. Bloom, D.H. Waldeck, Chiral electrocatalysts eclipse water splitting metrics through spin control, Nat. Commun. 14 (2023) 1067, https://doi.org/10.1038/s41467-023-36703-w.
[33] J. Li, J. Ma, Z. Ma, E. Zhao, K. Du, J. Guo, T. Ling, Spin effect on oxygen electrocatalysis, Adv. Energ. Sust. Res. 2 (2021) 2100034, https://doi.org/10.1002/aesr.202100034.
[34] B.P. Bloom, V. Kiran, V. Varade, R. Naaman, DavidH. Waldeck, Spin selective charge transport through cysteine capped CdSe quantum dots, Nano Lett. 16 (2016) 4583–4589, https://doi.org/10.1021/acs.nanolett.6b01880.
[35] Y. Adhikari, T. Liu, H. Wang, Z. Hua, H. Liu, E. Lochner, P. Schlottmann, B. Yan, J. Zhao, P. Xiong, Interplay of structural chirality, electron spin and topological orbital in chiral molecular spin valves, Nat. Commun. 14 (2023) 5163, https://doi.org/10.1038/s41467-023-40884-9.
[36] W. Chang, B. Qi, L. Jiang, Z. Li, G. Hu, Y. Yang, J. Li, Y. Zhao, Y.-F. Song, Two-dimensional confined polyoxometalate-based chiral electrode for high-performance enantioselective electrocatalytic oxidation, Chem Catal. 4 (2024), https://doi.org/10.1016/j.checat.2023.100859.
[37] L. Scarpetta-Pizo, R. Venegas, P. Barrías, K. Muñoz-Becerra, N. Vilches-Labbé, F. Mura, A.M. Méndez-Torres, R. Ramírez-Tagle, A. Toro-Labbé, S. Hevia, J. H. Zagal, R. Oñate, A. Aspée, I. Ponce, Electron spin-dependent electrocatalysis for the oxygen reduction reaction in a chiro-self-assembled iron phthalocyanine device, Angew. Chem. 136 (2024) e202315146, https://doi.org/10.1002/ange.202315146.
[38] G. Albano, A. Taddeucci, F. Zinna, L.A. Aronica, G. Pescitelli, L. Di Bari, Systematic investigation of optical and chiroptical properties of chiral π-conjugated oligomers in solution and thin films, Eur. J. Org. Chem. 27 (2024) e202400294, https://doi.org/10.1002/ejoc.202400294.
[39] Z. Bian, K. Kato, T. Ogoshi, Z. Cui, B. Sa, Y. Tsutsui, S. Seki, M. Suda, Hybrid chiral MoS2 layers for spin-polarized charge transport and spin-dependent electrocatalytic applications, Adv. Sci. 9 (2022) 2201063, https://doi.org/10.1002/advs.202201063.
[40] A. Olshtrem, I. Panov, S. Chertopalov, K. Zaruba, B. Vokata, P. Sajdl, J. Lancok, J. Storch, V. Církva, V. Svorcik, M. Kartau, A.S. Karimullah, J. Vana, O. Lyutakov, Chiral plasmonic response of 2D $Ti_3C_2T_x$ flakes: realization and applications, Adv. Funct. Mater. 33 (2023) 2212786, https://doi.org/10.1002/adfm.202212786.
[41] T. Feng, W. Chen, J. Xue, F. Cao, Z. Chen, J. Ye, C. Xiao, H. Lu, Spin polarization of chiral amorphous Fe-Ni electrocatalysts enabling efficient electrochemical oxygen evolution, Adv. Funct. Mater. 33 (2023) 2215051, https://doi.org/10.1002/adfm.202215051.
[42] D.H. Waldeck, R. Naaman, Y. Paltiel, The spin selectivity effect in chiral materials, APL Mater. 9 (2021) 040902, https://doi.org/10.1063/5.0049150.
[43] P. Vensaus, Y. Liang, N. Zigon, N. Avarvari, V. Mujica, G.J. Soler-Illia, M. Lingenfelder, Hybrid mesoporous electrodes evidence CISS effect on water oxidation, J. Chem. Phys. 160 (2024) 111103, https://doi.org/10.1063/5.0199339.
[44] L. Wang, W. Chen, D. Zhang, Y. Du, R. Amal, S. Qiao, J. Wu, Z. Yin, Surface strategies for catalytic CO_2 reduction: from two-dimensional materials to nanoclusters to single atoms, Chem. Soc. Rev. 48 (2019) 5310–5349, https://doi.org/10.1039/C9CS00163H.
[45] Q. Zuo, T. Liu, C. Chen, Y. Ji, X. Gong, Y. Mai, Y. Zhou, Ultrathin metal–organic framework nanosheets with ultrahigh loading of single Pt atoms for efficient visible-light-driven photocatalytic H2 evolution, Angew. Chem. Int. Ed. 58 (2019) 10198–10203, https://doi.org/10.1002/anie.201904058.
[46] F. Purcell-Milton, R. McKenna, L.J. Brennan, C.P. Cullen, L. Guillemeney, N. V. Tepliakov, A.S. Baimuratov, I.D. Rukhlenko, T.S. Perova, G.S. Duesberg, A. V. Baranov, A.V. Fedorov, Y.K. Gun'ko, Induction of chirality in two-dimensional nanomaterials: chiral 2D MoS_2 nanostructures, ACS Nano 12 (2018) 954–964, https://doi.org/10.1021/acsnano.7b06691.
[47] V. Kuznetsova, Y. Gromova, M. Martinez-Carmona, F. Purcell-Milton, E. Ushakova, S. Cherevkov, V. Maslov, Y.K. Gun'ko, Ligand-induced chirality and optical activity in semiconductor nanocrystals: theory and applications, Nanophotonics 10 (2021) 797–824, https://doi.org/10.1515/nanoph-2020-0473.
[48] K.-G. Zhou, F. Withers, Y. Cao, S. Hu, G. Yu, C. Casiraghi, Raman Modes of MoS2 Used as Fingerprint of van der Waals Interactions in 2-D Crystal-Based Heterostructures, ACS Nano 8 (2014) 9914–9924, https://doi.org/10.1021/nn5042703.
[49] H. Li, Q. Zhang, C.C.R. Yap, B.K. Tay, T.H.T. Edwin, A. Olivier, D. Baillargeat, From bulk to monolayer MoS_2: evolution of Raman scattering, Adv. Funct. Mater. 22 (2012) 1385–1390, https://doi.org/10.1002/adfm.201102111.
[50] C. Lee, H. Yan, L.E. Brus, T.F. Heinz, J. Hone, S. Ryu, Anomalous lattice vibrations of single- and few-layer MoS2, ACS Nano 4 (2010) 2695–2700, https://doi.org/10.1021/nn1003937.
[51] H.C. Woo, I.-S. Nam, J.S. Lee, J.S. Chung, K.H. Lee, Y.G. Kim, Room-temperature oxidation of $K_2CO_3MoS_2$ catalysts and its effects on alcohol synthesis from CO and H_2, J. Catal. 138 (1992) 525–535, https://doi.org/10.1016/0021-9517(92)90304-Z.
[52] K. Kleiner, C.A. Murray, C. Grosu, B. Ying, M. Winter, P. Nagel, S. Schuppler, M. Merz, On the origin of reversible and irreversible reactions in $LiNi_xCo_{(1-x)/2}Mn_{(1-x)/2}O_2$, J. Electrochem. Soc. 168 (2021) 120533, https://doi.org/10.1149/1945-7111/ac3c21.
[53] J. Fransson, L. Turin, Current induced spin-polarization in chiral molecules, J. Phys. Chem. Lett. 15 (2024) 6370–6374, https://doi.org/10.1021/acs.jpclett.4c01362.
[54] Z. Bian, Y. Nakano, K. Miyata, I. Oya, M. Nobuoka, Y. Tsutsui, S. Seki, M. Suda, Chiral van der waals superlattices for enhanced spin-selective transport and spin-dependent electrocatalytic performance, Adv. Mater. 35 (2023) 2306061, https://doi.org/10.1002/adma.202306061.
[55] P.K. Bhartiya, D. Mishra, Chiral-driven spin-based Ni/Al bifunctional Electrocatalyst, Appl. Surf. Sci. 655 (2024) 159661, https://doi.org/10.1016/j.apsusc.2024.159661.
[56] P.K. Bhartiya, M. Srivastava, D. Mishra, Chiral-induced enhanced electrocatalytic behaviour of cysteine coated bifunctional Au–Ni bilayer thin film device for water splitting application, Int. J. Hydrogen Energy 47 (2022) 42160–42170, https://doi.org/10.1016/j.ijhydene.2021.08.219.
[57] H. Lee, S. Ma, S. Oh, J. Tan, C.U. Lee, J. Son, Y.S. Park, J. Yun, G. Jang, J. Moon, Chirality-induced spin selectivity of chiral 2D perovskite enabling efficient spin-dependent oxygen evolution reaction, Small 19 (2023) 2304166, https://doi.org/10.1002/smll.202304166.
[58] X. Bai, Y. Cao, Y. Xu, W. Huang, P. Deng, X. Tian, Z. Liu, J. Wang, J. Tu, Enhanced photocatalytic hydrolysis performance of chiral molecule loaded titanium disulfide nanosheets, ChemPhysChem 23 (2022) e202200156, https://doi.org/10.1002/cphc.202200156.
[59] W. Zhang, C. Jiang, H. Guan, Y. Wang, Y. Hu, W. Wang, W. Tian, L. Hao, Unlocking OER catalytic potential and chiral Fe3O4 film as a game-changer for electrochemical water oxidation pathway and by-product control, Mater. Adv. 5 (2024) 1340–1347, https://doi.org/10.1039/D3MA00854A.
[60] S. Ghosh, B.P. Bloom, Y. Lu, D. Lamont, D.H. Waldeck, Increasing the efficiency of water splitting through spin polarization using cobalt oxide thin film catalysts, J. Phys. Chem. C 124 (2020) 22610–22618, https://doi.org/10.1021/acs.jpcc.0c07372.
[61] A.N. Nair, S. Fernandez, M. Marcos-Hernández, D.R. Romo, S.R. Singamaneni, D. Villagran, S.T. Sreenivasan, Spin-Selective oxygen evolution reaction in chiral iron oxide nanoparticles: synergistic impact of inherent magnetic moment and chirality, Nano Lett. 23 (2023) 9042–9049, https://doi.org/10.1021/acs.nanolett.3c02752.

[62] M. Ai, L. Pan, C. Shi, Z.-F. Huang, X. Zhang, W. Mi, J.-J. Zou, Spin selection in atomic-level chiral metal oxide for photocatalysis, Nat. Commun. 14 (2023) 4562, https://doi.org/10.1038/s41467-023-40367-x.
[63] F. Tassinari, K. Banerjee-Ghosh, F. Parenti, V. Kiran, A. Mucci, R. Naaman, Enhanced hydrogen production with chiral conductive polymer-based electrodes, J. Phys. Chem. C 121 (2017) 15777–15783, https://doi.org/10.1021/acs.jpcc.7b04194.
[64] J. Ran, M. Si, D. Gao, Co@CoO chiral nanostructures enabling efficient oxygen electrocatalysis by modulated spin-polarization, Chem. Eng. J. 493 (2024) 152545, https://doi.org/10.1016/j.cej.2024.152545.